RSC Advances

PAPER

View Article Online
View Journal | View Issue

Cite this: *RSC Adv.*, 2018, **8**, 36625

Construction of flower-like MoS_2/Fe_3O_4/rGO composite with enhanced photo-Fenton like catalyst performance†

Dongzhao Mu,‡ Zhe Chen, ‡* Hongfei Shi* and Naidi Tan*

High-performance and recyclable photocatalysts have attracted considerable amounts of attention for use in wastewater treatment. In this paper, a MoS_2/Fe_3O_4/rGO (0.1 wt%) composite was synthesized by an environmentally-friendly and facile strategy, and showed high potential for recyclability. The nanocomposite exhibited high photocatalytic activity in the presence of H_2O_2 and rGO (reduced graphene oxide) under visible-light irradiation. Notably, when 3 mg of MoS_2/Fe_3O_4/rGO (0.1 wt%) was added to rhodamine B (RhB, 30 mg L^{-1}) solution, the degradation rate was almost 100% within 40 min at neutral pH under visible-light irradiation. This rate was four times more rapid than that of MoS_2 and double that of MoS_2/Fe_3O_4. The results indicate that rGO plays an important role in photocatalysis by suppressing the recombination of photogenerated electron–hole pairs and enhancing the absorption capability of visible-light and organic dyes. Finally, the photocatalytic and stability mechanisms of MoS_2/Fe_3O_4/rGO (0.1 wt%) are proposed. This work further helps our understanding of the photo-Fenton mechanism. Furthermore, the synthesis of this composite has potential for application in energy storage devices.

Received 17th September 2018
Accepted 22nd October 2018

DOI: 10.1039/c8ra06537c

rsc.li/rsc-advances

Introduction

Environmental pollution and energy shortages are becoming increasingly serious problems of modern society.[1–4] In recent years, water pollution has been recognized as an important contributor to environmental pollution. Advanced oxidation processes (AOPs) are considered promising technologies for achieving environmental remediation.[5–10] Among different AOPs, Fenton oxidation technology has received much attention because of its simple technological requirements, cheap catalysts and effective removal of environmental pollutants.[11,12] However, the traditional homogenous Fenton process has the problems of secondary treatment, catalyst loss in effluent, and low pH (pH < 3.0) requirements, which greatly restrict its practical applications. Compared with the traditional Fenton reaction, "Fenton-like" reactions are now considered to be one of the most effective methods, as they can overcome the above-mentioned drawbacks.[13–20] Accordingly, the key issue is obtaining semiconducting, heterogeneous, Fenton-like catalysts with high stability, excellent activity, wide pH range and reusability.

Molybdenum sulfide (MoS_2), as an n-type semiconductor, has been widely studied in the fields of photocatalysis,[21,22] electrochemistry,[23] sensors,[24] supercapacitors,[25] and drug delivery[26] due to its high abundance, good crystallization, low cost, good conductivity, and large specific surface area. Therefore, much research effort has been devoted to constructing MoS_2-based materials through chemical vapor deposition, gas-phase synthesis, heterostructural engineering, hydrothermal methods, and thermal decomposition. These methods have produced materials such as MoS_2/Bi_2WO_6,[27] MoS_2/TiO_2,[28] CdS/MoS_2,[29,30] graphene/MoS_2,[31,32] MoS_2/C_3N_4,[33] MoS_2/Ag_3PO_4,[34] and MoS_2/Co_3O_4.[35] There is currently very few studies on preparing ternary heterostructure nanocomposite photocatalysts.

Recently, magnetite (Fe_3O_4) has been widely investigated and extensively applied in biomedicine, photocatalysis, therapeutics, and lithium-ion batteries[36–43] owing to its good conductivity, easy collectability, strong adsorption, high stability, and high theoretical capacity. Many studies have reported that it shows promise for application in Fenton/photo-Fenton reactions due to containing ferrous Fe(II) and ferric Fe(III), and producing efficient Fenton reagents under illumination. Therefore, superparamagnetic ferric oxide (Fe_3O_4) is considered to be an ideal candidate for a magnetic catalyst. In addition, Fe_3O_4 has good electrical conductivity, which can rapidly improve the efficiency of electron/hole separation. Thus, it has recently been found that the performance of photocatalysis can be improved. Meanwhile, by introducing external magnetics, the recycling of catalysts has been improved at the same time,

School of Science, Jilin Institute of Chemical Technology, Jilin 132022, PR China. E-mail: chenzhecz999@163.com

† Electronic supplementary information (ESI) available: The *k* values of different samples in the photocatalytic process. See DOI: 10.1039/c8ra06537c

‡ These authors contributed equally.

which is beneficial for practical applications. However, some results demonstrate that magnetite materials usually operate in acidic conditions; furthermore, because of the low surface area of this material, Fe ions can leach into the reaction solution. Hence, combinations with other visible-light-driven semiconductor photocatalytic materials have attracted considerable attention, because they can enhance stability, improve photocatalytic activity, and allow easy separation and recycling. Han *et al.* prepared a MoS_2/Fe_3O_4 nanocomposite by a hydrothermal method.[44] Xu *et al.* developed Fe_3O_4/g-C_3N_4 composites with good photocatalytic activity through a simple electrostatic self-assembly method.[45] However, the preparation of these ternary photocatalysts usually requires a multistep process and relatively harsh reaction conditions.

In this study, we report, for the first time, a facile and cost-effective approach to the large-scale synthesis of the ternary photocatalyst MoS_2/Fe_3O_4/rGO (0.1 wt%) under simple hydrothermal conditions. Compared with MoS_2/Fe_3O_4 and pure MoS_2, the MoS_2/Fe_3O_4/rGO (0.1 wt%) composite exhibits both a large specific surface area and good photocatalytic activity in the photo-degradation of rhodamine (B) in the presence of H_2O_2 and rGO under visible-light irradiation. In addition, the experiment reveals that, on the one hand, the rGO creates an MoS_2/Fe_3O_4 hybrid, which can accelerate the separation and transfer of photogenerated electron–hole pairs, which improves photocatalytic activity; on the other hand, hydrogen peroxide (H_2O_2) produces strong oxidative capacity, whereby ·OH and $\cdot O^{2-}$ radicals enhance the degradation efficiency of rhodamine (RhB) at neutral pH. The stability and possible mechanisms of the as-prepared MoS_2/Fe_3O_4/rGO are also explored. Our research opens a new door for the practical utilization of photo-degradation. Furthermore, this magnetic material may have potential practical use in sensors and for energy storage.

Experimental

Synthesis and characterization

Ferric chloride hexahydrate ($FeCl_3$), sodium acetate (NaAc), polyvinylpyrrolidone (PVP k30), sodium molybdate (Na_2MoO_4) and L-cysteine were obtained from Sinopharm Chemical Reagent Co., Ltd. (Shanghai, China) and used without further purification. Distilled water was used in all experiments. Reduced graphene oxide nanosheets were purchased from Nanjing XFNANO Materials Technology Corporation Ltd., Nanjing, China. Monodispersed Fe_3O_4 nanoparticles were prepared according to previous literature.[46] In brief, monodispersed Fe_3O_4 (10 mg) nanoparticles were dispersed in 60 mL of distilled water under ultrasonic radiation for 20 min. Afterward, 0.121 g Na_2MoO_4 and 0.121 g L-cysteine were added slowly into the above solution under mechanical stirring at room temperature. After 30 min of stirring, a certain amount of rGO (0.25 mg mL^{-1}) suspension was added dropwise under stirring. The mixture was transferred into an 80 mL Teflon-lined stainless-steel autoclave and heated to 180 °C for 24 h. The autoclave was allowed to cool to room temperature, the black precipitate was separated and washed by distilled water several times, and then washed with ethanol. Finally, the resulting products were dried at 60 °C overnight.

X-ray diffraction (XRD) measurements were carried out by an X-ray powder diffractometer (Rigaku, Japan) equipped with a CuKα source (λ = 0.15418 nm). X-ray photoelectron spectroscopy (XPS) was performed using a JEOL2010F instrument. The morphologies and microstructures of the samples were observed by scanning electron microscopy (SEM; S-4800, Hitachi), transmission electron microscopy (TEM) and high-resolution transmission electron microscopy (HRTEM; JEM-2100, Japan). The Brunauer–Emmett–Teller (BET) specific surface areas (S_{BET}) of the samples were measured through nitrogen adsorption by Micromeritics (ASAP 2020M, USA). Fourier transform infrared (FTIR) spectra of the as-prepared samples were measured on a PerkinElmer Spectrum One spectrometer in the range 4000–400 cm^{-1} with the KBr tabletting method.

Photocatalytic performance measurements

The photocatalytic efficiencies of the obtained samples were evaluated by the degradation of RhB in the presence of H_2O_2 under visible-light irradiation supplied by an 800 W Xe-lamp (Phchem III, Beijing NBET Technology Co., Ltd, λ > 420 nm). In a typical photocatalytic degradation experiment, 3 mg of MoS_2/Fe_3O_4/rGO was dispersed in 50 mL RhB (30 mg L^{-1}) solution under magnetic stirring for 10 min at room temperature. Before irradiation, the suspensions were magnetically stirred for another 50 min in darkness to ensure the establishment of an adsorption–desorption equilibrium, and then 30 wt% of H_2O_2 was added to the above suspensions. During the photocatalytic tests, 3 mL of the suspensions were taken out at given time intervals and magnetically separated to remove the catalyst completely. The concentration of RhB was measured by a UV-Vis spectrophotometer (UV-3600, Shimadzu) at λ_{max} = 554 nm. The catalytic activities were calculated by the formula $E = C_0 - C_t/C_0 \times 100\%$, where C_0 and C_t represent the adsorption equilibrium absorbance of RhB and the desired time intervals, respectively. To detect the major active species in the photo Fenton-like process, radical-trapping experiments were conducted. The hydroxyl radical (·OH) scavenger, superoxide anion radical ($\cdot O_2^-$), and hole (h^+) scavenger can usually be trapped by isopropanol (IPA), 4-hydroxy-TEMPO, and triethanolamine (TEOA), respectively. Typically, different scavengers were dispersed into the suspension solutions before the photocatalytic tests, and the following procedure was similar to the RhB degradation process.

Results and discussion

Materials characterizations

To confirm the crystallographic phases of the as-prepared samples, X-ray diffraction patterns of the precursors were obtained (Fig. 1). The pattern of pure Fe_3O_4 exhibited six typical peaks, located at 30.1, 35.5, 43.1, 53.4, 57.0 and 62.6°, which can be ascribed to the {220}, {311}, {400}, {422}, {511} and {440} facets of cubic Fe_3O_4 (JCPDS card no. 17-0320), respectively. For

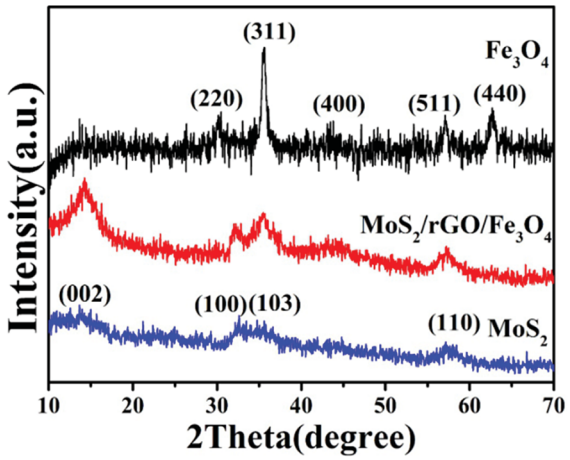

Fig. 1 XRD patterns of MoS_2, Fe_3O_4 and MoS_2/Fe_3O_4/rGO (0.1 wt%).

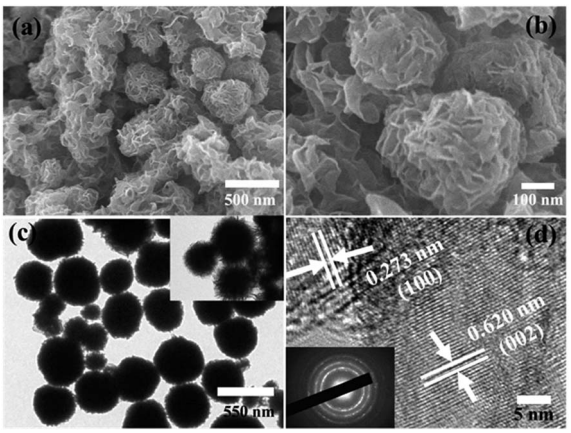

Fig. 3 SEM images (a and b), and TEM images low and high magnifications (c and d) of MoS_2/Fe_3O_4/rGO (0.1 wt%).

the pattern of pure MoS_2, only three characteristic peaks appeared at about $2\theta = 14.4°$ {002}, 32.7° {100}, 39.5° {103} and 58.3° {110}, respectively, which can be assigned to the database of the hexagonal phase of MoS_2 (JCPDS card no. 37-1492). Compared with pure MoS_2 and Fe_3O_4, the dominant peaks of MoS_2 could be indexed in the XRD spectrum of MoS_2/Fe_3O_4/rGO, while there was low diffraction intensity of Fe_3O_4, and no peaks for rGO were detected due to the small amounts of Fe_3O_4 (12 wt%) and rGO (0.5 wt%). Therefore, this suggests that no other impurity-related diffraction peaks were present, indicating that the desired MoS_2/Fe_3O_4/rGO (0.1 wt%) composites were successfully prepared and closely combined using the hydrothermal method.

To further test the purity and elemental composition of the MoS_2/Fe_3O_4/rGO (0.1 wt%) material, XPS analysis was carried out. From Fig. 2a, it can be seen that the elements C, N, O, Mo, Fe, and S coexist in the sample, which is consistent with the XRD results. The peaks obtained at 284.8, 286.0, 287.5 and 288.9 eV are associated with the binding energies of sp^2 C–C, C–O, C=O and O=C–O bonds, respectively (Fig. 2b).[47,48] Fig. 2c shows the high-resolution XPS spectrum of Fe 2p. The Fe $2p_{3/2}$ and Fe $2p_{1/2}$ peak positions at 707.5 eV and 719.6 eV are characteristic of unoxidized Fe in the sample, while the peaks at 711.2 eV (Fe $2p_{3/2}$) and 724.6 eV (Fe $2p_{1/2}$) correspond to Fe^{3+}, as reported in the literature.[49,50] The peaks of the O 1s (Fig. 2d) XPS spectrum at 530.3, 531.2 and 532.2 eV are in accordance with Fe–O (O^{2-}), OH^- and H_2O.[51] The peak of Mo3d (Fig. 2e) can be fitted by three peaks corresponding to 228.6 eV (Mo $3d_{5/2}$), 231.7 (Mo $3d_{3/2}$) and 226.1 eV (Mo–S bond).[52] This suggests that elemental Mo exists in the composite as Mo^{4+}. Additionally, three high-resolution spectral peaks of S 2p with shake-up satellites were detected, which are characteristic of S $2p_{3/2}$ (161.5 eV) and S $2p_{1/2}$ (162.6 eV), while another peak at 164.1 eV indicated the presence of S–C bonds. These results are close to those reported in previous literature.[53–55]

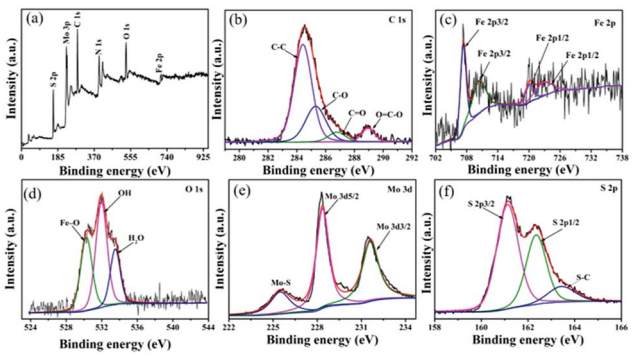

Fig. 2 XPS spectra of MoS_2/Fe_3O_4/rGO (1 wt%): (a) the full survey; (b) C 1s (c) Fe 2p (d) O 1s (e) Mo 3d; (f) S 2p.

The morphology and crystal structures of the as-prepared samples were investigated by SEM and TEM (Fig. 3). Fig. 3a and b are typical low- and high-magnification SEM images of the as-prepared samples. The MoS_2/Fe_3O_4/rGO (0.1 wt%) material exhibited hierarchical flower-like microspheres with mean diameters in the range 1–1.5 μm. Further observation showed that the as-prepared sample still had uniformly dispersed flower-like microspheres composed of intercrossed nanosheets with thicknesses of 2–5 nm. A TEM image was made to confirm the morphology and microstructure of the MoS_2/Fe_3O_4/rGO (0.1 wt%) composites. As shown in Fig. 3c, the MoS_2/Fe_3O_4/rGO (0.1 wt%) composites were highly uniform flower-like spheres with mean diameters of 1–1.5 μm, which agrees well with that observed by SEM. To investigate the crystalline structure, HRTEM images were recorded (Fig. 3d). The HRTEM image recorded on the edge of a single MoS_2/Fe_3O_4/rGO (0.1 wt%) nanoflower shows lattice distances of 0.62 and 0.26 nm, which corresponds to the *d*-spacing of (002) and (100) crystal planes. In addition, the selected area electron diffraction (SAED) pattern indicates the polycrystalline nature of the MoS_2/Fe_3O_4/rGO material.

The FTIR spectra of as-prepared photocatalyst samples in the range of 500–4000 cm^{-1} are shown in Fig. 4. It can be clearly seen that the OH groups were observed and located broadly around 3400 cm^{-1} in the FTIR spectra, which can be attributed to the stretching and bending vibrations of water molecules adsorbed on the samples. Compare with MoS_2 and MoS_2/Fe_3O_4, the characteristic peaks at 1642 cm^{-1} and 1566 cm^{-1} correspond to the C=O of stretching COOH groups and aromatic

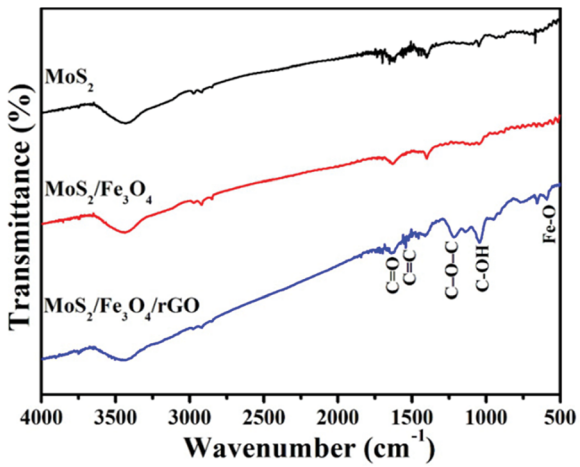

Fig. 4 FTIR spectra of MoS_2, MoS_2/Fe_3O_4 and MoS_2/Fe_3O_4/rGO (0.1 wt%).

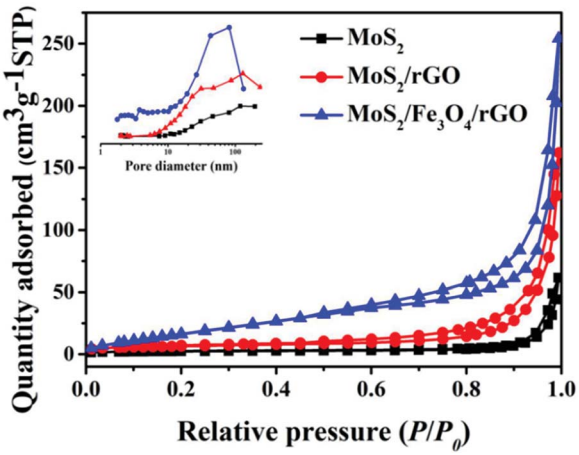

Fig. 5 N_2 adsorption–desorption isotherms and pore-size distribution curves of the obtained samples.

C=C bonds, respectively, while the absorption peaks at 1219 cm^{-1} and 1044 cm^{-1} accord with epoxy groups (C–O–C group vibrations) and alkoxy groups (C–OH), respectively.[56] In addition, the intensive band at 588 cm^{-1} in the MoS_2/Fe_3O_4/rGO (0.1 wt%) spectrum can also be attributed to the Fe–O stretching vibration mode.[57] All of these results indicate the presence of rGO in the composites.

To investigate the physicochemical properties of different samples, the as-prepared heterogeneous samples were subject to N_2 adsorption–desorption analysis. Fig. 5 shows the N_2 adsorption/desorption isotherm and the pore-size distribution (inset) of as-prepared samples, which reveals that all of the samples were type-IV isotherms with an H3-type hysteresis loop, and exhibited mesoporous distribution. Compared to MoS_2 and MoS_2/Fe_3O_4, the MoS_2/Fe_3O_4/rGO (0.1 wt%) sample had a specific surface area of 72.23 $m^2\ g^{-1}$ and a pore volume of 0.185 $cm^3\ g^{-1}$, which are in agreement with the SEM and TEM results (Table 1). In summary, the high specific surface area provides more active sites, which may lead to the enhancement of photocatalytic performance.

Table 1 The corresponding physicochemical properties of as-prepared samples

Sample	Average crystal size [nm] (standard deviation)	S_{BET} [$m^2\ g^{-1}$]	Pore volume [$cm^3\ g^{-1}$]
MoS_2	18.22	8.16	0.04
MoS_2/Fe_3O_4	21.32	22.59	0.12
MoS_2/Fe_3O_4/rGO	10.27	72.23	0.185

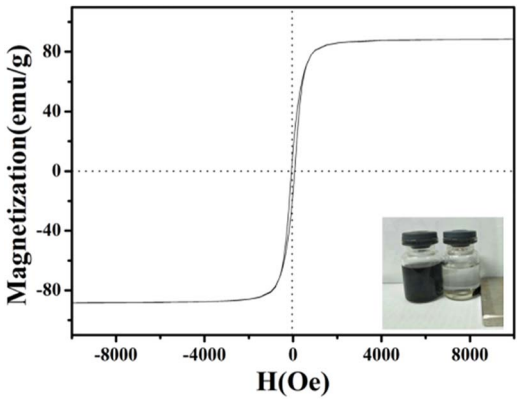

Fig. 6 Hysteresis curves of MoS_2/Fe_3O_4/rGO (0.1 wt%) composites.

The magnetic properties of MoS_2/Fe_3O_4/rGO (0.1 wt%) were analyzed at room temperature, as shown in Fig. 6. The saturation magnetization (M_s) value of 87 emu g^{-1} demonstrates its excellent magnetic properties, allowing it to be easily separated from the treated samples by an external magnet within 10 min. The time-dependent degradation intensity change of MoS_2/Fe_3O_4/rGO (0.1 wt%) is shown in Fig. 7a. It can be seen that the main absorption peak of MoS_2/Fe_3O_4/rGO (0.1 wt%) located at 554 nm rapidly diminished in the presence of H_2O_2 under visible-light irradiation for 40 min. Notably, this result was also consistent with a color change of the sample, from pink to colorless, as shown in the inset in Fig. 7a. In order to investigate the photocatalytic behavior of MoS_2/Fe_3O_4/rGO (0.1 wt%), a series of comparative experiments were carried out, as shown in Fig. 7b and S1.† It shows that before visible-light irradiation, the mixed suspension containing the catalyst and RhB was continually stirred in darkness for 30 min to ensure that the rhodamine B was attached to the surface of the catalyst until reaching adsorption equilibrium. Due to its variable surface areas, the adsorption capacity of RhB onto the catalyst surface (in darkness) ranged from 2.7% to 22.1% of C/C_0. Compared with MoS_2/Fe_3O_4 and pure MoS_2, the MoS_2/Fe_3O_4/rGO (0.1 wt%) material exhibited the best photocatalytic activity in terms of the photo-degradation of rhodamine (B) in the presence of H_2O_2 under visible-light irradiation. This was almost four times higher than that of MoS_2 and double that of MoS_2/Fe_3O_4. These observations demonstrate that rGO plays an important role in enhancing catalytic activity because it can provide a larger specific surface area, abundant active sites, high visible-light absorption, and improves the separation efficiency of photo-generated electron–hole pairs. However, the catalyst

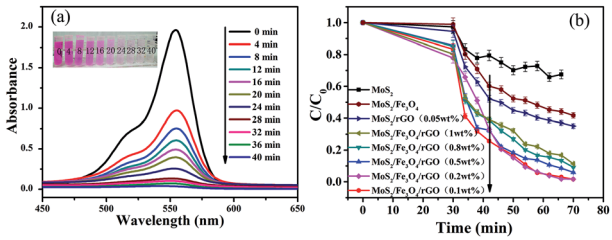

Fig. 7 UV-spectra of absorption of degradation (a) MoS_2/Fe_3O_4/rGO (0.1 wt%) and degradation curves of different samples (the amount of H_2O_2: 100 μL) (b). Error bars representing standard deviation are calculated at 95% confidence level.

degradation rate decreased with increases in the concentration of graphene from 0.2 wt% to 1 wt%, which was attributed to its shielding of light absorption and decreases of active sites.

In order to investigate the effects of pH and H_2O_2 volume on the degradation of RhB in the photo-Fenton reaction, a series of comparative experiments were performed under visible-light irradiation while holding other conditions constant. Fig. 8a shows the effect of pH on RhB degradation resulting from experiments conducted in acidic, neutral and alkaline media. The pH values were adjusted by adding NaOH (1 mol L^{-1}) and HCl (1 mol L^{-1}) to the solutions. As the pH of the solutions increased from 2.5 to 7, it was easily found that the RhB degradation efficiency reached almost 100% in the presence of H_2O_2 under visible-light irradiation. It is well known that the traditional homogenous Fenton process suffers from secondary treatment, catalyst loss in effluent, and the requirement for low pH (<3.0) conditions; however, the photocatalytic rate did not decrease when using the neutral media in our experiment. This suggests that this photocatalytic material may have potential practical use for industrial wastewater treatment systems. In contrast, the degradation rate decreased as the pH of the solution increased to 9, which indicates that ≡Fe(IV)═O species or high-valent iron species of $\equiv Fe^{IV}$═O were formed, which further reduced the degradation activity of the reaction at alkaline pH values.[58] The results of these experiments indicate that pH has a significant influence on the photocatalytic degradation of RhB.

In addition, to further explore whether H_2O_2 can affect the efficiency of photocatalytic degradation, the experiment was performed with different volumes of H_2O_2 at pH 7 under visible-light irradiation (Fig. 8b). With the addition of various volumes

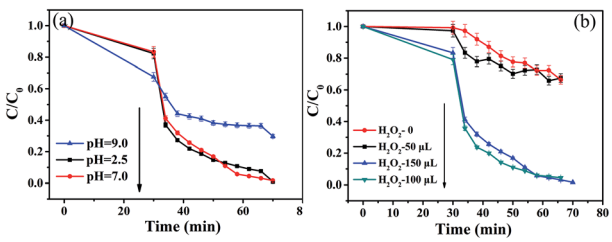

Fig. 8 Photocatalytic degradation of RhB by the as-prepared MoS_2/Fe_3O_4/rGO (0.1 wt%) samples with different value of pH (the amount of H_2O_2: 100 μL) (a) and different volume of H_2O_2 (b). Error bars representing standard deviation are calculated at 95% confidence level.

of H_2O_2 (30%), from 0 to 150 μL, into the solution, the degradation rates were calculated to be 32.5%, 33.6%, 99.8% and 95.6%, respectively. The degradation rate increased with enhancing volume of H_2O_2. Therefore, introduction of H_2O_2 is credited with enhancing the RhB degradation rate, which produced more and more ·OH which then reacted with catalyst. In addition, it can be seen that the photocatalytic activity slightly decreased with H_2O_2 (30%) additions of up to 150 μL into the solution, which was possibly due to the quenching of ·OH by competing reactions between H_2O_2 and ·OOH.[59]

To consider the practical application of these photocatalysts, recycling tests were conducted under visible-light irradiation, as shown in Fig. 9a. Under the same conditions as the photo Fenton-like reaction, an RhB degradation rate of >90% was observed after five successive cycles using the same experimental conditions. This indicates that the MoS_2/Fe_3O_4/rGO (0.1 wt%) catalyst has high stability and reusability. Furthermore, the catalyst can be easily separated for reuse with an external magnet, which is especially important for practical applications such as industrial wastewater treatment. In order to confirm this photo Fenton-like reaction, free-radical and hole-trapping experiments were conducted in the presence of H_2O_2 (Fig. 9b). The degradation efficiency of RhB decreased to 31.02% when IPA was added, implying that ·OH species have an obvious role in the degradation of RhB. Compared with IPA, a slight decrease in the degradation rate was observed when TEOA and 4-hydroxy-TEMPO were added to the photocatalytic reaction system. Hence, it was also apparent that the photocatalytic activity of MoS_2/Fe_3O_4/rGO (0.1 wt%) was promoted, which was ascribed to the elimination/active decomposition of H_2O_2, namely, by the generation of active ·OH radicals. It was identified that ·OH radicals play a major role in the photo Fenton-like reaction. To further confirm the effects of the photo Fenton-like reaction, experiments were performed where RhB was degraded under various conditions (Fig. 9c). Notably, it is

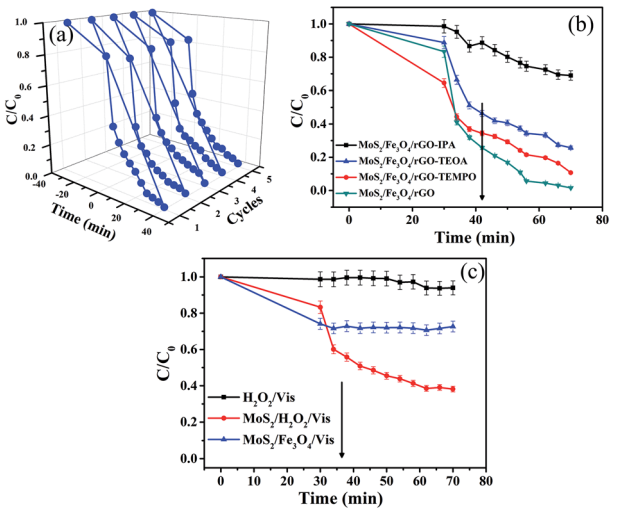

Fig. 9 Recycle experiments of (a) photodegradation of RhB with MoS_2/Fe_3O_4/rGO (0.1 wt%), the effects of various scavengers on photocatalytic activity of photocatalyst (b) and photo-Fenton degradation of RhB in different condition (c). Error bars representing standard deviation are calculated at 95% confidence level.

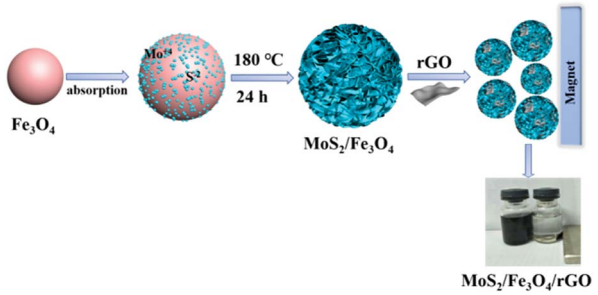

Fig. 10 Schematic illustration of the proposed formation mechanism of as-prepared samples.

believed that both H_2O_2 and Fe_3O_4 are crucial for enhancing the degradation of RhB in photo Fenton-like reactions.

Next, a possible photocatalytic mechanism is proposed for understanding photo Fenton-like reactions in the presence of H_2O_2 under visible-light irradiation. Firstly, the degradation products are quickly absorbed onto the catalyst due to graphene having a high surface area and active adsorption sites. Meanwhile, MoS_2/Fe_3O_4/rGO (0.1 wt%) composites are photo-excitable and generate electron–hole pairs. The photo-generated e^- rapidly react with Fe^{3+} to form Fe^{2+}. Secondly, the photogenerated electrons can be directly trapped by O_2/H_2O_2 to form $\cdot O_2^-$/$\cdot$OH. Simultaneously, Fe^{2+} can react quickly with H_2O_2 to generate $\cdot$OH species for organic degradation, forming the photo-Fenton system. Likewise, photogenerated holes can directly react with RhB. As a result, $\cdot OH/h^+/\cdot O_2^-$ reactive species would be used for the photodegradation of RhB *via* a photo Fenton-like system (Fig. 10).

$$MoS_2/Fe_3O_4/rGO + h\nu \rightarrow e^- + h^+ \quad (1)$$

$$Fe^{3+} + e^- \rightarrow Fe^{2+} \quad (2)$$

$$H_2O_2 + Fe^{2+} \rightarrow Fe^{3+} + \cdot OH + OH^- \quad (3)$$

$$\cdot OH + RhB = H_2O + CO_2 \quad (4)$$

Conclusions

In summary, this is the first report of a facile and cost-effective approach to the large-scale synthesis of ternary photocatalysts made from MoS_2/Fe_3O_4/rGO (0.1 wt%) under simple hydrothermal conditions. Their superior performance is attributed to a photo Fenton-like system. We found that rGO played an important role in the experiments, as it suppressed the recombination of photogenerated electron–hole pairs and enhanced the absorption capability of visible-light and organic dyes. Additionally, hydroxyl radicals ($\cdot$OH) and photogenerated holes exhibited strong abilities to degrade organic contaminants under the photo Fenton-like system. Finally, the photocatalyst can be effectively separated for reuse by simply applying an external magnetic field, which is especially important for industrial wastewater treatment.

Conflicts of interest

There are no conflicts to declare.

Acknowledgements

This work was supported by Science Technology Development Planning of Jilin Province (20170520069JH) and Education Department Project of Jilin Province (JJKH20180556KJ).

References

1 E. M. Dias and C. Petit, *J. Mater. Chem. A*, 2015, **3**, 22484–22506.
2 C. Cao, L. Xiao, C. Chen and Q. Cao, *Appl. Surf. Sci.*, 2015, **333**, 110–118.
3 L. Liang, Q. Zhu, T. Wang, F. Wang, J. Ma, L. Jing and J. Sun, *Microporous Mesoporous Mater.*, 2014, **197**, 221–228.
4 J. S. Kim, B. Kim, H. Kim and K. Kang, *Adv. Energy Mater.*, 2018, **8**, 1702774.
5 J. Y. Choe, J. Y. Byun and S. H. Kim, *Appl. Catal., B*, 2018, **233**, 272–280.
6 G. X. Zong, H. Chen, R. J. Qu, C. H. Wang and N. Y. Ji, *J. Hazard. Mater.*, 2011, **186**, 614–621.
7 D. F. Xu, B. Cheng, S. W. Cao and J. G. Yu, *Appl. Catal., B*, 2015, **164**, 380–388.
8 P. F. Xia, B. C. Zhu, B. Cheng, J. G. Yu and J. S. Xu, *ACS Sustainable Chem. Eng.*, 2018, **6**, 965–973.
9 X. Liu, H. Chen, C. H. Wang, R. J. Qu, C. N. Ji, C. M. Sun and Y. Zhang, *J. Hazard. Mater.*, 2010, **175**, 1014–1021.
10 S. W. Cao, F. Tao, Y. Tang, Y. T. Li and J. G. Yu, *Chem. Soc. Rev.*, 2016, **45**, 4747–4765.
11 M. A. Oturan and J. J. Aaron, A Review, *Crit. Rev. Environ. Sci. Technol.*, 2014, **44**, 2577–2641.
12 A. M. Khan, A. Mehmood, M. Sayed, M. F. Nazar, B. Ismail, R. A. Khan, H. Ullah, H. M. Abdur Rehman, A. Y. Khan and A. R. Khan, *J. Mol. Liq.*, 2017, **236**, 395–403.
13 L. Clarizia, D. Russo, I. Di Somma, R. Marotta and R. Andreozzi, *Appl. Catal., B*, 2017, **209**, 358–371.
14 X. X. Hua, R. Li, S. Y. Zhao and Y. J. Xing, *Appl. Surf. Sci.*, 2017, **396**, 1393–1402.
15 X. J. Guo, K. B. Wang, D. Li and J. B. Qin, *Appl. Surf. Sci.*, 2017, **420**, 792–801.
16 Y. Y. Liu, W. Jin, Y. P. Zhao, G. S. Zhang and W. Zhang, *Appl. Catal., B*, 2017, **206**, 642–652.
17 H. F. Wang, Y. G. Xu, L. Q. Jing, S. Q. Huang, Y. Zhao, M. Q. He, H. Xu and H. M. Li, *J. Alloys Compd.*, 2017, **710**, 510–518.
18 G. Ayoub and A. Ghauch, *Chem. Eng. J.*, 2014, **256**, 280–292.
19 A. Ghauch, G. Ayoub and S. Naim, *Chem. Eng. J.*, 2013, **228**, 1168–1181.
20 A. Ghauch and H. Baydoun, *Chem. Eng. J.*, 2011, **172**, 18–27.
21 W. Z. Fu, X. W. Xu, W. B. Wang, J. F. Shen and M. X. Ye, *ACS Sustainable Chem. Eng.*, 2018, **6**, 8935–8944.
22 M. Li, D. G. Wang, J. H. Li, Z. D. Pan, H. J. Ma, Y. X. Jiang, Z. J. Tian and A. H. Lu, *Chin. J. Catal.*, 2017, **38**, 597–606.

23 J. Yan, Z. G. Chen, H. Y. Ji, Z. Liu, X. Wang, Y. G. Xu, X. J. She, L. Y. Huang, L. Xu, H. Xu and H. M. Li, *Chem.–Eur. J.*, 2016, **22**, 4764–4773.
24 M. Park, Y. J. Park, X. Chen, Y. K. Park, M. S. Kim and J. H. Ahn, *Adv. Mater.*, 2016, **28**, 2556–2562.
25 S. C. Zhang, R. R. Hu, P. Dai, X. X. Yu, Z. L. Ding, M. Z. Wu, G. Li, Y. Q. Ma and C. J. Tu, *Appl. Surf. Sci.*, 2017, **396**, 994–999.
26 W. Yin, L. Yan, J. Yu, G. Tian, L. Zhou, X. Zheng, X. Zhang, Y. Yong, J. Li, Z. Gu and Y. Zhao, *ACS Nano*, 2014, **8**, 6922–6933.
27 Y. M. Liu, Y. F. Cao, H. Lv, S. Li and H. Zhang, *Mater. Lett.*, 2017, **188**, 99–102.
28 W. Zhou, Z. Yin, Y. Du, X. Huang, Z. Zeng, Z. Fan, H. Liu, J. Wang and H. Zhang, *Small*, 2013, **9**, 140–147.
29 D. A. Reddy, J. Choi, S. Lee, Y. J. Kim, S. Hong, D. P. Kumara and T. K. Kim, *Catal. Sci. Technol.*, 2016, **6**, 6197–6206.
30 Y. Min, G. He, Q. Xu and Y. Chen, *J. Mater. Chem. A*, 2014, **2**, 2578–2584.
31 C. Zhao, X. Wang, J. Kong, J. M. Ang, P. S. Lee, Z. Liu and X. Lu, *ACS Appl. Mater. Interfaces*, 2016, **8**, 2372–2379.
32 H. Zhao, H. Zeng, Y. Wu, S. Zhang, B. Li and Y. Huang, *J. Mater. Chem. A*, 2015, **3**, 10466–10470.
33 J. Yan, Z. G. Chen, H. Y. Ji, Z. Liu, X. Wang, Y. G. Xu, X. J. She, L. Y. Huang, L. Xu, H. Xu and H. M. Li, *Chem.–Eur. J.*, 2016, **22**, 4764–4773.
34 Y. H. Song, Y. C. Lei, H. Xu, C. Wang, J. Yan, H. Z. Zhao, Y. G. Xu, J. X. Xia, S. Yin and H. M. Li, *Dalton Trans.*, 2015, **44**, 3057–3066.
35 D. Z. Zhang, C. X. Jiang, P. Li and Y. Sun, *ACS Appl. Mater. Interfaces*, 2017, **9**, 6462–6471.
36 C. Y. Wang, L. Y. Zhang, S. N. Li, M. J. Zhang, T. T. Wang, L. Li, C. G. Wang and Z. G. Su, *J. Mater. Chem. B*, 2016, **4**, 5809–5813.
37 D. Lin, X. Feng, Y. N. Wu, B. D. Ding, T. Lu, Y. B. Liu, X. B. Chen, D. Chen and C. H. Yang, *Appl. Surf. Sci.*, 2018, **436**, 140–146.
38 K. Y. Li, Y. Q. Zhao, M. J. Janik, C. S. Song and X. W. Guo, *Appl. Surf. Sci.*, 2017, **396**, 1383–1392.
39 S. Valizadeh, M. H. Rasoulifard and M. S. SeyedDorraji, *Appl. Surf. Sci.*, 2014, **319**, 358–366.
40 F. Chai, K. Li, C. Song and X. Guo, *J. Colloid Interface Sci.*, 2016, **475**, 119–125.
41 D. Du, W. Shi, L. Wang and J. Zhang, *Appl. Catal., B*, 2017, **200**, 484–492.
42 L. L. Chen, L. Li, T. T. Wang, L. Y. Zhang, S. X. Xing, C. G. Wang and Z. M. Su, *Nanoscale*, 2014, **6**, 6603–6608.
43 B. Q. Liu, Q. Zhang, Z. S. Jin, L. Y. Zhang, L. Li, Z. G. Gao, C. G. Wang, H. M. Xie and Z. M. Su, *Adv. Energy Mater.*, 2017, 1702347.
44 C. L. Han, G. R. Huang, D. J. Zhu and K. H. Hu, *Mater. Chem. Phys.*, 2017, **200**, 16–22.
45 S. Sahar, A. Zeb, Y. N. Liu, N. Ullah and A. W. Xu, *Chin. J. Catal.*, 2017, **38**, 2110–2119.
46 H. Deng, X. Li, Q. Peng, X. Wang, J. Chen and D. Y. Li, *Angew. Chem., Int. Ed.*, 2005, **117**, 2842–2845.
47 E. Vishnyakova, B. E. Brinson, L. B. Alemany, M. Verma and W. E. Billups, *Chem.–Eur. J.*, 2016, **22**, 1452–1460.
48 Y. Li, H. Zhang, Y. Wang, P. Liu, H. Yang, X. Yao, D. Wang, Z. Tang and H. Zhao, *Energy Environ. Sci.*, 2014, **7**, 3720–3726.
49 S. W. Li, Y. C. Wang, S. J. Peng, L. J. Zhang, A. M. Al-Enizi, H. Zhang, X. H. Sun and G. F. Zheng, *Adv. Energy Mater.*, 2016, **6**, 1501661.
50 R. H. Huang, Z. Q. Fang, X. M. Yan and W. Cheng, *Chem. Eng. J.*, 2012, **197**, 242–249.
51 K. Fan, Y. F. Ji, H. Y. Zou, J. F. Zhang, B. C. Zhu, H. Chen, Q. Daniel, Y. Luo, J. G. Yu and L. C. Sun, *Angew. Chem., Int. Ed.*, 2017, **56**, 1–6.
52 H. B. Geng, J. Yang, Z. F. Dai, Y. Zhang, Y. Zheng, H. Yu, H. W. Wang, Z. Z. Luo, Y. Y. Guo, Y. F. Zhang, H. S. Fan, X. L. Wu, J. W. Zheng, Y. G. Yang, Q. Y. Yan and H. W. Gu, *Small*, 2017, 1603490.
53 B. B. Wang, Y. Zhang, J. Zhang, R. Y. Xia, Y. L. Chu, J. C. Zhou, X. W. Yang and J. Huang, *ACS Appl. Mater. Interfaces*, 2017, **9**, 12907–12913.
54 M. Choi, S. K. Koppala, D. Yoon, J. H. wang, S. M. Kim and J. Kim, *J. Power Sources*, 2016, **309**, 202–211.
55 W. S. V. Lee, E. Peng, T. A. J. Loh, X. Huang and J. M. Xue, *Nanoscale*, 2016, **8**, 8042–8047.
56 J. F. Shen, Y. Z. Hu, M. Shi, N. Li, H. W. Ma and M. X. Ye, *J. Phys. Chem. C*, 2010, **114**, 1498–1503.
57 X. Yang, X. Zhang, Y. Ma, Y. Huang, Y. Wang and Y. Chen, *J. Mater. Chem.*, 2009, **19**, 2710.
58 L. Ren, S. Y. Lu, J. Z. Fang, Y. Wu, D. Z. Chen, L. Y. Huang, Y. F. Chen, C. Cheng, Y. Liang and Z. Q. Fang, *Catal. Today*, 2017, **281**, 656–661.
59 F. X. Wang, Y. L. Chen, R. S. Zhu and J. M. Sun, *Dalton Trans.*, 2017, **47**, 11306–11317.